Nature of active sites in Ni$_2$P hydrotreating catalysts as probed by iron substitution

Haiyan Zhao [a,b], S. Ted Oyama [a,c,*], Hans-Joachim Freund [d], Radosław Włodarczyk [e], Marek Sierka [f]

[a] Department of Chemical Engineering, Virginia Tech, Blacksburg, VA 24061, USA
[b] Department of Chemical Engineering, University of Idaho, Idaho Falls, ID 83402, USA
[c] Department of Chemical Systems Engineering, The University of Tokyo, 7-3-1 Hongo, Bunkyo-ku, Tokyo 113-8656, Japan
[d] Department of Chemical Physics, Fritz Haber Institute of the Max Planck Society, Faradayweg 4-6, Berlin 14195, Germany
[e] Institut für Chemie, Humboldt-Universität zu Berlin, Unter den Linden 6, 10099 Berlin, Germany
[f] Otto-Schott-Institut für Materialforschung, Friedrich-Schiller-Universität Jena, Löbdergraben 32, D-07743 Jena, Germany

ARTICLE INFO

ABSTRACT

A series of NiFeP/SiO$_2$ catalysts with different Ni:Fe molar ratios (1:0, 3:1, 1:1, 1:3, 0:1) was investigated for the hydrodesulfurization (HDS) of 4,6-dimethyldibenzothiophene. The Fe component is a good probe for active sites because Ni$_2$P and Fe$_2$P adopt the same hexagonal crystal structure, yet Fe$_2$P is completely inactive for HDS. X-ray diffraction analysis and FTIR spectroscopy of adsorbed CO indicated the formation homologous alloys. At 3.1 MPa and 613 K (340 °C) the activity of the alloys was similar to that of Ni$_2$P, which was very high. There was also unprecedented selectivity toward direct desulfurization (DDS). A reconstruction of the NiFe phase occurred to expose more Ni sites, likely driven by the formation of surface Ni-S bonds as observed by EXAFS. The analysis showed that Ni(2) pyramidal sites responsible for hydrogenation were largely replaced by Fe. This left behind Ni(1) tetrahedral sites which favor DDS and explains the reactivity results.

© 2014 Elsevier B.V. All rights reserved.

1. Introduction

The removal of sulfur from petroleum is important for producing clean transportation fuels and is an area of active research [1,2]. The US Environmental Protection Agency recently issued a final rule requiring refineries to cut sulfur levels in gasoline from 30 ppm to 10 ppm by Jan. 2017 [3]. Current topics of study include investigation of the nitrogen tolerance [4], trimetallic compositions [5], the addition of additives like P and B [6] and Ga [7], the use of egg-shell or hierarchical supports [8], the use of composite supports [9,10], the use of zeolites [11], the use of mesoporous supports [12,13], oxidative desulfurization [14], and noble metals [15]. Metal phosphides have recently received extensive attention as a new type of hydrodesulfurization (HDS) catalyst because of their high activity and stability in the HDS and hydrodenitrogenation (HDN) of model and real feeds [8,16–22]. In initial studies it was reported that the activity of common phosphides follows the order:

Ni$_2$P > WP > MoP > CoP > Fe$_2$P in the simultaneous HDS of dibenzothiophene (3000 ppm S) and HDN of quinoline (2000 ppm N) at 643 K (370 °C) and 3.1 MPa, with the comparison based on equal sites (240 µmol CO chemisorption for phosphides) [23,24]. A number of bimetallic phosphides such as Ni$_x$Mo$_y$P [25–30], Co$_x$Mo$_y$P [31] and Ni$_x$Co$_y$P [32,33] have also been studied because a synergistic effect between the components was foreseen as found for promoted metal sulfides. Unexpectedly, however, these bimetallic phosphide phases did not show enhanced activity over the component Ni, Co or Mo phosphides, except for the case of Co$_x$Ni$_y$P [20] where a 50% increase in conversion was found.

The high activity of Ni$_2$P has prompted many studies of its synthesis, structure [34], and reactivity. The crystal structure of Ni$_2$P is the same as that of Fe$_2$P with space group P$\bar{6}$2m, and the hexagonal unit cell contains two types of Ni atoms, Ni(1) of tetrahedral coordination and Ni(2) of square pyramidal coordination (Fig. 1a). These sites are also denoted T and SP sites. Viewed from the c-axis the structure can be understood as originating from layers of hexagonal T and SP arrays (Fig. 1b). There have been a number of studies of Ni$_2$P by ab initio methods [35] and density functional theory (DFT) [36,37] A recent DFT study of Ni$_2$P reports that Ni sites in threefold hollows and neighboring P atoms are responsible for adsorption
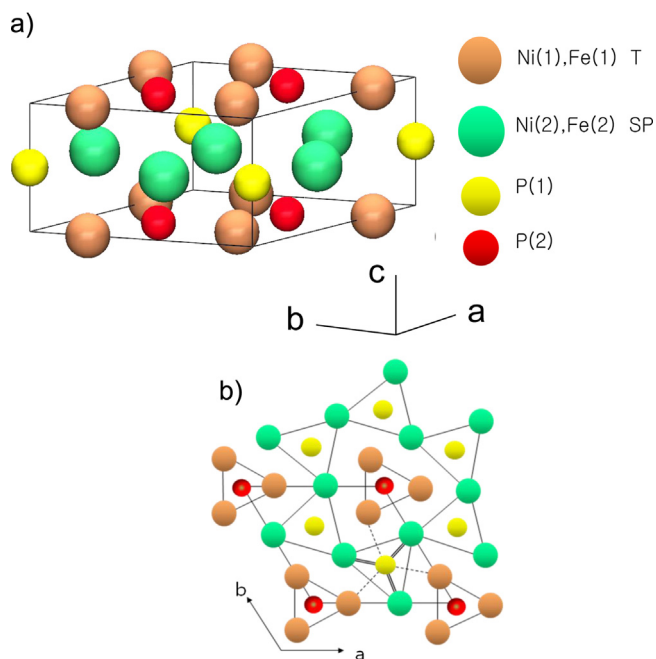
Fig. 1. Fe_2P and Ni_2P crystal structure with symmetry equivalent sites (Refs. [10,11]). Metal atoms occupy tetrahedral (T) sites (orange) and square pyramidal (SP) sites (green), while phosphorus atoms are located in P_1 and P_2 sites. (a) Unit cell. (b) Top view showing two hexagonal layers in the c direction. (For interpretation of the references to color in this figure legend, the reader is referred to the web version of this article.)

of H and OH [38]. In the present work DFT is used to examine the energetics of substitution of Fe for Ni in the Ni_2P lattice, and it is found that the energy differences are small.

A recent study indicated that the pyramidal Ni(2) type was particularly active for HDS by the hydrogenation route [39]. The compound Fe_2P is isostructural with Ni_2P [40,41], and it was of interest to study NiFeP alloys because Fe_2P itself has very low activity, so in a preliminary study by the authors it was surmised that substitution of Fe for Ni could provide confirmation of the role of the two types of Ni atoms [42]. This work extends the previous study. In order to gain insight into the nature of the surface active sites Fourier transform infrared (FTIR) spectroscopy is employed using CO as the probe molecule. Extended X-ray absorption fine structure (EXAFS) measurements are carried out to elucidate the structure of the alloy formed by substitution of the Fe atom in the active phase.

2. Experimental

2.1. Materials

The support fumed silica EH-5 (Surface area = 350 $m^2\,g^{-1}$) was provided by Cabot Corp. The chemicals used in the synthesis of the catalysts were $Fe(NO_3)_3\cdot9H_2O$ (Aldrich, 99%), Ni $(NO_3)_2\cdot6H_2O$ (Alfa Aesar, 99%), $(NH_4)_2HPO_4$ (Aldrich, 99%). The chemicals utilized in the reactivity study were 4,6-dimethyldibenzothiophene (synthesized, 95%), dimethyl disulfide (Acros Organics, 99%), quinoline (Aldrich, 98%), tetralin (Aldrich, 97%), n-octane (Acros Organics, 99%), and n-tridecane (Alfa Aesar, 99%). The gases employed were H_2 (Airco, Grade 5, 99.99%), He (Airco, Grade 5, 99.99%), CO (Linde Research Grade, 99.97%), 0.5% O_2/He (Airco, UHP Grade, 99.99%), O_2 (Airco, UHP Grade, 99.99%), 10% H_2S/H_2 (Airco, UHP Grade, 99.99%) and N_2 (Airco, Grade 5, 99.99%).

2.2. Synthesis

The NiFeP catalysts were prepared by temperature-programmed reduction (TPR), following procedures reported previously [43,44]. Briefly, the synthesis of the catalysts involved two stages. First, solutions of the corresponding metal phosphate precursors were prepared by dissolving appropriate amounts of $Fe(NO_3)_3\cdot9H_2O$, $Ni(NO_3)_2\cdot6H_2O$, with ammonium phosphate in distilled water, and these solutions were used to impregnate silica EH-5 by the incipient wetness method. The obtained samples were dried and calcined at 500 °C for 6 h, then ground with a mortar and pestle, pelletized with a press (Carver, Model C), and sieved to particles of 650–1180 μm diameter (16/20 mesh). Second, the solid phosphates were reduced to phosphides at 2 °C min^{-1} in flowing H_2 [1000 cm^3 (NTP) $min^{-1}\,g^{-1}$]. The reduction temperatures were 825 K (552 °C) for Ni_2P/SiO_2, 835 K (562 °C) for $NiFeP(3:1)/SiO_2$, 840 K (567 °C) for $NiFeP(1:1)/SiO_2$, 845 K (572 °C) for $NiFeP(1:3)/SiO_2$ and for Fe_2P/SiO_2. The samples were kept at the reduction temperatures for 2 h, followed by cooling to room temperature under He flow [100 cm^3 (NTP) min^{-1}], and then passivated at room temperature in a 0.5% O_2/He for 4 h. The total metal molar loading was 1.6 mmol g^{-1} (mmol per g of support) in all cases and the metal to phosphorus ration in the precursor is 1:2. Compositions prepared were Ni_2P/SiO_2, $NiFeP(3:1)/SiO_2$, $NiFeP(1:1)/SiO_2$, $NiFeP(1:3)/SiO_2$, and Fe_2P/SiO_2, where the numbers in parenthesis are molar ratios. The overall weight loadings for all of the metal phosphide catalysts were very close around 8 wt.% (see Table 3).

2.3. Characterization

Temperature-programmed reduction (TPR) was carried out on pelletized catalyst samples (typically 0.2 g) placed in quartz U-tube reactors. The samples were heated with linear temperature ramps in flowing hydrogen to reduce the metal phosphate to metal phosphide. The temperature was increased from room temperature to 973 K (700 °C) at 2 °C with a hydrogen flow rate of 200 cm^3 (NTP) min^{-1}. A portion of the exit gas flow was sampled through a leak valve into a mass spectrometer and the masses 2 (H_2), 18 (H_2O), 31 (P) and 34 (PH_3) were monitored during the experiment and used to decide the optimal reduction temperature.

Irreversible CO uptake measurements were used to titrate the surface metal atoms and to provide an estimate of the active sites on the catalysts for the transition metal phosphides. Usually, 0.3 g of a passivated sample was loaded into a quartz reactor. The passivated transition metal phosphides were reduced at 450 °C for 2 h. After cooling in He, pulses of CO in a He carrier at 65 cm^3 (NTP) min^{-1} were injected at room temperature through a sampling valve, and the mass 28 (CO) signal was monitored with mass spectrometer. CO uptake was calculated by measuring the decrease in the peak areas caused by adsorption in comparison with the area of the calibrated volume of 19.5 μmol gas.

Surface areas of the samples were obtained using the BET method based on adsorption isotherms at liquid nitrogen temperature, and using a value of 0.162 nm^2 for the cross-sectional area of a N_2 molecule. The measurements were performed in a volumetric adsorption unit (Micromeritics ASAP 2000). X-ray diffraction (XRD) patterns of the samples were obtained with a Scintag XDS-2000 powder diffractometer operated at 45 kV and 40 mA, using Cu Kα monochromatized radiation (λ = 0.154178 nm). The crystallite size of the supported samples was calculated using the Scherrer equation, $D_c = K\lambda/\beta\cos(\theta)$, where K is a constant as 0.9, λ is the wavelength of the X-ray radiation, β is the peak width in radians at half-maximum, corrected for instrumental broadening (0.1°), and 2θ is the Bragg angle.

X-ray absorption spectra at the Ni K-edge (8.333 keV) and Fe K-edge (7.112 keV) of reference and catalyst samples were recorded in the energy range 8.233–9.283 keV at beam line X18B at the National Synchrotron Light Source at Brookhaven National Laboratory. The X-ray ring at the National Synchrotron Light Source has a flux of 1×10^{10} photons s^{-1} at 100 mA and 2.5 GeV. The monochromator is equipped with a Si(1 1 1) channel-cut single crystal and has an energy range capability of 5.8–40 keV. The crystal was detuned slightly to prevent glitches due to harmonics. EXAFS spectra were recorded at ambient temperature in transmission mode using ionization chambers for the detection of primary (I_0, 100% N$_2$) and transmitted (I_t, 75% N$_2$, balance Ar) beam intensities.

Samples before reaction (labeled as fresh) were reduced in hydrogen as for the reactivity studies, and were loaded into cells with Kapton windows without exposure to the atmosphere. Samples after reaction (denoted as spent) were removed from the reactor and placed in a hexane solvent and washed and dried before being transferred to the EXAFS cell, all without exposure to air. Bulk reference samples were diluted with BN (0.1 g cat + 0.3 g BN). The EXAFS data were reduced and analyzed by the program Athena and Artemis [45]. To fit the experimental EXAFS spectra for the fresh and spent samples, theoretical EXAFS models were constructed from the software FEFF8 [46] based on the crystal structures of Ni$_2$P and Fe$_2$P [44]. The Fourier transform (FT) spectra are shown without phase correction. The FT of the measured spectra was fitted with a k-weight of 1, 2, and 3. The FT figures of the experimental and modeling data are shown with the data processed with a k-weight of 3.

The EXAFS data from the supported Ni$_2$P and Fe$_2$P were transformed over the data range from 20 to 120 nm^{-1} and modeled in the region from 0.1 to 0.3 nm^{-1}. The EXAFS models based on the crystal structures of Ni$_2$P and Fe$_2$P contains parameters: energy shift values, coordination number values, σ^2. The quantity Reff is the initial reference half path length (bond length for single scattering path) as calculated by FEFF. The EXAFS best-fit values for the half path lengths (R) and σ^2 are listed in Tables S5–S8 (Supplementary information). Multi-edge fittings were carried out for the samples NiFeP(3:1)/SiO$_2$, NiFeP(1:1)/SiO$_2$, NiFeP(1:3)/SiO$_2$. For the spent and fresh NiFeP(1:1)/SiO$_2$, difference spectra of the raw absorption data between spent and fresh samples were obtained to show the presence of a small oscillation.

2.4. Reactivity studies

Hydrotreating activities of the samples were measured in a three-phase, packed-bed reactor operated at 3.1 MPa and 613 K (340 °C) with a model feed liquid containing 500 ppm sulfur as 4,6-DMDBT, 3000 ppm sulfur as dimethyl disulfide, 200 ppm nitrogen as quinoline, 1 wt.% tetralin, 0.5 wt.% n-octane as internal standard, and balance n-tridecane. Lack of mass and heat transfer limitations was ascertained by making sure that the Weisz-Prater and Mears criteria were satisfied (Supplementary Information). The schematic of the testing system was described in an earlier paper [47]. Briefly, the testing unit consisted of three parallel reactors immersed in a fluidized sand bath (Techne, Model SBL-2) whose temperature was controlled by a temperature controller (Omega, Model 6015 K). The reactors were 19 mm/16 mm (o.d./i.d.) 316 stainless steel tubes with central thermocouples monitoring the temperature of the catalyst. The catalysts were in the form of pellets (16/20 mesh), and were supported between quartz wool plugs in a 13 mm i.d. 316 stainless steel basket. The hydrogen flow rate was set to 100 μmol s^{-1} (150 cm^3 min^{-1}, NTP) with a mass flow controller (Brooks, Model 5850E), and the feed liquid was injected by a high-pressure liquid pump (LDC Analytical, Model NCI 11D5) at a flow rate of 5 cm^3 h^{-1}. Quantities of catalysts loaded in the reactors corresponded to the same amount of CO uptake (240 μmol).

Table 1
Ni$_2$P, Fe$_2$P lattice parameters (nm).

	a	b	c
Ni$_2$P	0.5859	0.5859	0.3382
Fe$_2$P	0.5867	0.5867	0.3458

Table 2
d-Spacing of the three strongest peaks of XRD for NiFeP/SiO$_2$ samples.

Reflection plane (hkl)	(1 1 1) (°)
Ni$_2$P/SiO$_2$	40.9
NiFeP(3:1)/SiO$_2$	41.1
NiFeP(1:1)/SiO$_2$	40.8
NiFeP(1:3)/SiO$_2$	40.8
Fe$_2$P/SiO$_2$	40.2

The weight of the catalysts used for reactivity test is reported in Table S2 in the supplemental information. The LHSVs for the 5 catalysts Ni$_2$P/SiO$_2$, NiFeP(3:1)/SiO$_2$, NiFeP(1:1)/SiO$_2$, NiFeP(1:3)/SiO$_2$, and Fe$_2$P/SiO$_2$ are 1.6 h^{-1}, 1.4 h^{-1}, 0.8 h^{-1}, 0.7 h^{-1}, and 0.8 h^{-1}, respectively. Prior to the reactivity testing, the catalysts were pretreated in H$_2$ at 723 K (450 °C) for 2 h. Hydrotreating products were collected every few hours in sealed septum vials and were analyzed by a gas chromatograph (Hewlett-Packard, 5890A) equipped with a 0.32 mm i.d. × 50 m fused silica capillary column (CPSIL-5CB, Chrompack, Inc.) and a flame ionization detector.

2.5. CO-FTIR

Transmission infrared spectra of pressed wafers (~50 mg) of catalysts were collected in situ in a reactor cell placed in a Fourier transform infrared (FTIR) spectrometer (Bio-Rad Model FTS 3000MX) at a resolution of 4 cm^{-1} and using 64 scans spectrum. The IR cell was equipped with water-cooled KBr windows, connections for inlet and outlet flows, and thermocouples to monitor and control the temperature. Before dosing CO, the samples were reduced in H$_2$ at 723 K (450 °C) for 2 h at the same conditions used for CO chemisorption and reactivity studies, then cooled to room temperature in a He flow and exposed to CO until saturation was achieved. The samples were then purged in He carrier for 300 s to remove gaseous and weakly adsorbed CO species. The spectra were obtained in the absorbance mode and are shown after subtraction of a background spectrum obtained on the freshly reduced samples to make the spectral features more clear.

2.6. Computational details

Periodic density functional theory (DFT) calculations were carried out using the Vienna Ab Initio Simulation package (VASP) [48,49] and the Perdew, Burke and Ernzerhof (PBE) exchange-correlation functional [50]. The calculations were performed using the projector augmented wave method (PAW), originally developed by Blöchl [51] and adapted by Kresse and Joubert [52]. Only the valence electrons were explicitly considered. Optimizations of cell parameters used a $7 \times 7 \times 13$ Monkhorst-Pack k-point mesh [53] for the Brillouin-zone sampling and an energy cutoff of 1000 eV for a plane wave basis set. The Pulay stress arising from the incomplete basis set was minimized by restarting the optimization until self-consistency of the total energy was reached. Optimizations of atomic positions for the structures shown in Table 1 were performed with a $4 \times 4 \times 7$ Monkhorst-Pack k-point mesh and a plane wave cutoff of 400 eV. Optimizations of atomic positions for the structures shown in Table 2 were performed with a plane wave cutoff of 500 eV. Optimizations of atomic positions for $1 \times 1 \times 2$ supercells were performed with $4 \times 4 \times 4$ Monkhorst-Pack k-point mesh.
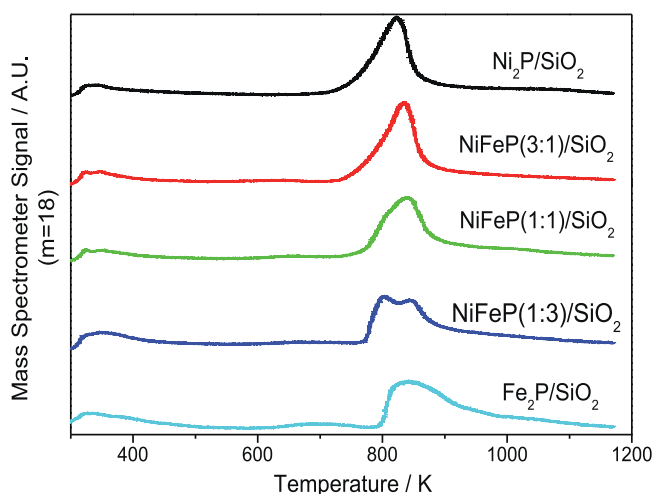
Fig. 2. Temperature programmed reduction of Ni_2P, Fe_2P and NiFeP samples (mass 18 signal).

Fig. 3. X-ray diffraction patterns for reduced Ni_2P, Fe_2P and NiFeP samples.

3. Results and discussion

3.1. Temperature-programmed reduction

The supported nickel-iron phosphides were prepared in two stages as described in the experimental part. First, solutions of the nickel-iron and phosphorous components were impregnated on the silica support and the materials were dried to form supported phosphate precursors. Second, the phosphates were transformed into phosphides by temperature-programmed reduction (TPR). The TPR experiments were carried out to understand the phenomena involved in the reduction process and to determine the optimum reduction conditions used for large scale catalyst preparation.

Fig. 2 shows mass 18 for the water evolution during the temperature programmed reduction for the $NiFeP/SiO_2$ precursors with various Ni to Fe ratios. Here only water evolution is shown because the other masses provided little additional information. The TPR peak for Fe_2P/SiO_2 is wider than that of Ni_2P/SiO_2 and has a trailing at high-temperature side which indicates that Fe_2P is intrinsically more difficult to reduce than Ni_2P and thus is probably more heterogeneously dispersed. With increasing Fe contents, the TPR traces showed more peaks and a more complicated overall reduction pattern than that of the higher Ni content samples. When Fe reached 75% for the sample with Ni to Fe ratio 1:3, two distinct TPR peaks were observed. One peak is very close to the peak temperature of iron phosphide, the other one overlaps the initial nickel phosphate reduction temperature. As the Ni/Fe ratio decreases (1:0, 3:1, 1:1, 1:3, 0:1), the reduction peaks for NiFeP catalysts shift to higher temperature from 825 to 845 K (552–572 °C). These temperatures were chosen for the NiFeP precursor reduction with the corresponding Ni/Fe ratio to make sure NiFeP catalysts were fully reduced at the same time to minimize particles sintering.

3.2. X-ray diffraction analysis

X-ray diffraction (XRD) measurements were taken for reduced NiFeP catalysts with various Ni/Fe ratio (Fig. 3). The diffraction pattern for iron phosphide shows a high background because of fluorescence of the iron. The standard patterns from the powder diffraction file for Ni_2P and Fe_2P are very similar as Ni_2P and Fe_2P both adopt the same hexagonal structure (space group: $P\bar{6}2m$ $P\bar{6}2m$, barringerite shown in Fig. 1) [54]. Table 1 lists the lattice parameters of Ni_2P and Fe_2P, and as can be seen they are close, with the Fe_2P unit cell being slightly larger than that of Ni_2P. As a
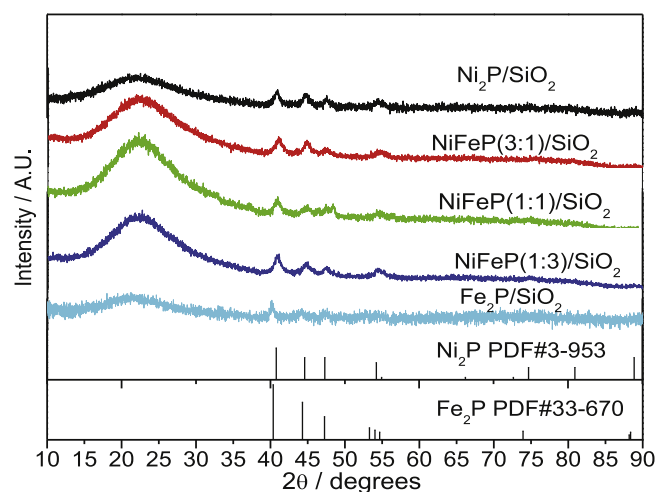
result, the five silica supported samples Ni_2P/SiO_2, $NiFeP(3:1)/SiO_2$, $NiFeP(1:1)/SiO_2$, $NiFeP(1:3)/SiO_2$, and Fe_2P/SiO_2 showed very similar XRD patterns as well (Fig. 3). Compared with the standard powder diffraction files for Ni_2P and Fe_2P, the NiFe samples, $NiFeP(3:1)/SiO_2$, $NiFeP(1:1)/SiO_2$ and $NiFeP(1:3)/SiO_2$ show XRD patterns that are closer to that of Ni_2P. This suggests the new phases preferentially to remain more like the Ni_2P phase. Table 2 lists the positions for the (1 1 1) reflection varied with NiFe ratios. The (1 1 1) reflection locates at 40.9° for Ni_2P supported on silica and at 40.2° for the supported Fe_2P. The (1 1 1) reflection is observed at 40.8° for NiFeP with Ni/Fe ratio 1/3 while then increases anomalously to 41.1° for NiFeP with more Ni content (Ni/Fe ratio 3/1), which is even larger than that for the supported Ni_2P. Thus, the lattice parameters for the NiFeP metal alloys which change nonlinearly with the compositions do not follow Vegard's Law. This result is consistent with the study from Fruchart [55]. The $NiFeP(3:1)/SiO_2$ observed with the highest Bragg angle for the (1 1 1) reflection has minimum unit cell volume. This trend is obeyed with the observation that the hexagonal system $(Fe_{1-x}Ni_x)_2P$ has the minimum volume at the composition $x = 0.85$ [55,56]. The crystallite sizes were also calculated from the XRD line-broadening using the Scherrer equation. The supported NiFeP catalysts had crystallite sizes about 10 nm closer to the Ni_2P crystallite size but much smaller than that for Fe_2P.

3.3. CO chemisorption and BET results

The CO chemisorption and BET characterization results are reported in Table 3. The specific surface areas of the supported materials were around 130–150 $m^2\,g^{-1}$ much lower than that of the support (SiO_2, 350 $m^2\,g^{-1}$), which was caused by the sintering during synthesis process. The CO chemisorption results of the samples are reported in the third column of Table 3. Ni_2P/SiO_2 has the largest CO uptake among this series of catalysts while Fe_2P/SiO_2 has a much lower CO uptake value. As the iron content increased in the bimetallic phosphides, the CO uptake values decreased steadily. The uptake of $NiFeP(1:3)/SiO_2$ even went below that of Fe_2P/SiO_2. The dispersion (D) of the metal sites was estimated from the CO uptakes and the known loading of the samples (in all cases 1.6 mmol g^{-1} of total metal). The particle size (d) was then calculated using the equation $d \approx 0.9/D$. The dispersion of the mixed NiFe samples decreased with iron content following the trend in the CO uptake. The Ni_2P/SiO_2 and Fe_2P/SiO_2 samples show good agreement between the particle size obtained from chemisorption and from line-broadening, which indicates that these two methods work consistently for estimation

Table 3
Characterization of NiFeP/SiO$_2$ samples.

Sample	Loading (wt.%)	BET surface area (m^2 g^{-1})	CO uptake (μmol g^{-1})	Dispersion (%)	Particle size[a] (nm)	Crystallite size[b] (nm)
Ni$_2$P/SiO$_2$	7.92	135	110	10	9	10
NiFeP(3:1)/SiO$_2$	7.85	138	96	8	11	7
NiFeP(1:1)/SiO$_2$	7.78	153	60	5	18	9
NiFeP(1:3)/SiO$_2$	7.71	126	32	3	33	7
Fe$_2$P/SiO$_2$	7.64	148	52	4	20	21

[a] The particle size estimated by 0.9/D based on the CO chemisorption.
[b] The crystallite sizes estimated by the Scherrer equation based on the XRD line-broadening.
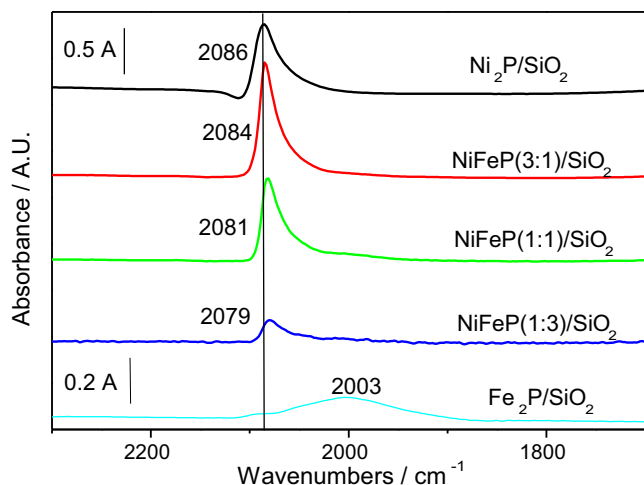
Fig. 4. Infrared spectra of adsorbed CO on reduced Ni$_2$P/SiO$_2$, NiFeP(3:1)/SiO$_2$, NiFeP(1:1)/SiO$_2$, NiFeP(1:3)/SiO$_2$ and Fe$_2$P/SiO$_2$.

Table 4
Infrared spectroscopy data for reduced transition metal phosphides and bimetallic phosphides.

Sample	ν_{CO} (cm^{-1})	Relative CO site intensity[a]	CO uptake (μmol g^{-1})
Ni$_2$P/SiO$_2$	2086	1.6	110
NiFeP(3:1)/SiO$_2$	2084	1.1	96
NiFeP(1:1)/SiO$_2$	2081	0.9	60
NiFeP(1:3)/SiO$_2$	2079	0.3	32
Fe$_2$P/SiO$_2$	2003	0.2	52

[a] Integrated absorbance/mg catalyst.

of monometallic phosphide particles. The samples containing more Fe show larger particle sizes estimated by chemisorption, which suggests that crystallites are agglomerated into polycrystalline particles. The formation of larger particles reduces both the CO uptakes and the dispersion.

3.4. Infrared spectroscopy of adsorbed CO

Studies of IR spectra for adsorbed CO are useful for characterizing the bonding properties of transition metal species [57–59]. Fourier transform infrared (FTIR) spectroscopy of adsorbed CO was used as a probe for surface structure and chemistry. Fig. 4 shows room temperature FTIR spectra of adsorbed CO in He flow on Ni$_2$P/SiO$_2$, NiFeP(3:1)/SiO2, NiFeP(1:1)/SiO2, NiFeP(1:3)/SiO$_2$ and Fe$_2$P/SiO$_2$. The first four catalysts share the same absorbance unit scale while the intensity for Fe$_2$P/SiO$_2$ was enlarged 2.5 times. The CO band position and integrated band intensity was summarized in Table 4.

Four types of bonding are reported for CO on Ni$_2$P: (1) CO adsorbed on Ni bridge sites (1914 cm^{-1}), (2) Ni(CO)$_4$ adsorbed on the surface of the catalyst (~2056 cm^{-1}), (3) CO adsorbed on atop Ni sites (2083–2093 cm^{-1}), and (4) P=C=O species on surface P

atoms (2177–2187 cm^{-1}). The characteristic band at 2086 cm^{-1} is attributed to CO on atop Ni sites on the surface of reduced Ni$_2$P/SiO$_2$ [60,61]. The low frequency and high stability of the IR band has been due to π back bonding to the antibonding orbitals of CO by d-electrons of the reduced Ni species.

The CO absorbance on Fe$_2$P/SiO$_2$ was observed at a substantially lower frequency of 2003 cm^{-1} with much lower intensity and a considerably broader peak. The observed frequency of 2003 cm^{-1} is much lower than that expected for a simple linear CO molecule on a metal phosphide. For example, in Co$_2$P/SiO$_2$ the CO band appears at 2062 cm^{-1} [56]. It is also higher than that found for bridged CO species, for example, 1919 cm^{-1} on Ni$_2$P [61]. Although multiple CO adsorption is not commonly reported for metallic Fe in NiFe alloys [62], in the case of Fe$_2$P, the Fe–Fe distance is larger than in metallic Fe which may allow for multiple CO molecules to adsorb on a single site. The best documented case for multiple CO adsorption is for Rh [63], where a gem-dicarbonyl species is formed. The vibrational frequency of the gem-dicarbonyl is lower than that of the linear single carbonyl and has contribution from symmetric and asymmetric modes. This, in addition to a distribution of sites, may account for the breadth of the CO mode observed on Fe$_2$P/SiO$_2$ (Fig. 4). Thus, the red-shift and broadening of the CO FTIR signal for the Fe$_2$P/SiO$_2$ sample is consistent with multiple adsorption on the metal centers as indicated by the CO chemisorption results, due to the formation of crystallites with different habits and exposed faces than those of Ni$_2$P/SiO$_2$ and its alloys.

The CO stretching frequency monotonically shifted to lower wavenumbers with increasing Fe content (Table 4) indicating the CO bond was weakened. This is possibly due to the electron donation from Fe to Ni, which would weaken the CO bond by backdonation to its antibonding orbitals. The electron donation from Fe to Ni was also proved by careful XPS and XANES measurements for the (Ni$_x$Fe$_{(1-x)}$)$_2$P [64]. Net electron donation from Fe to Ni is counterintuitive as Ni has more d electrons than Fe, however Ni has larger electronegativity (1.91) than Fe (1.81) and Ni has higher electron affinity (112 kJ/mol) than Fe (15.7 kJ/mol), so the Blyholder CO wavenumber shift to lower values is reasonable. Addition of the Fe component helps increase the electron density on Ni, which leads to stronger backbonding and improvement of the catalysts' performance as has been suggested that the higher electron density on the metal atom could improve HDS activity by increasing the dissociation of H$_2$ and the adsorption of thiophenes [65,66]. It should be noted that DFT calculations indicate that there is little charge transfer between Ni and P [27].

The CO peak intensity (I in absorbance units per mg) decreased with Fe content, indicating that the surface was increasingly occupied by Fe, which as a phosphide does not chemisorb CO appreciably. A comparison between the CO uptake by chemisorption and the CO relative intensity by FTIR is also reported in Table 4. The results are consistent for Ni$_2$P/SiO$_2$, NiFeP(3:1)/SiO$_2$, NiFeP(1:1)/SiO$_2$, and NiFeP(1:3)/SiO$_2$ since the CO uptake and relative intensity decrease in the same order. However, Fe$_2$P/SiO$_2$ is an exception: the CO uptake for Fe$_2$P/SiO$_2$ is close to that of NiFeP(1:1)/SiO$_2$ but the CO relative density measured by FTIR is the lowest among this series of catalysts. This could be due to a
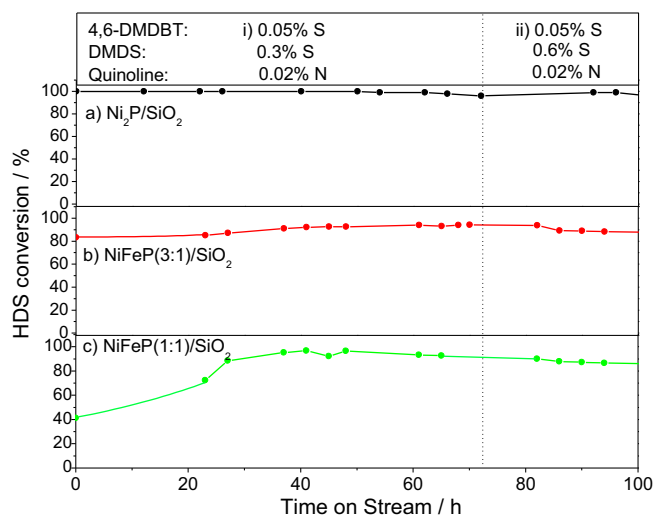
Fig. 5. Activity test at 340 °C in the HDS of 4,6-DMDBT for Ni$_2$P/SiO$_2$, NiFeP(3:1)/SiO$_2$ and NiFeP(1:1)/SiO$_2$.

much lower extinction coefficient for multiple CO bonding than for linear CO.

3.5. Reactivity tests

Reactivity studies of simultaneous 4,6-dimethyldibenzo-thiophene (4,6-DMDBT) HDS and quinoline HDN were carried out at 613 K (340 °C) at a pressure of 3.1 MPa (450 psig). Lack of mass and heat transfer limitations was verified by carrying out Weisz-Prater and Mears criteria calculations (Supplementary Information). Fig. 5 shows the 4,6-DMDBT conversion for the Ni$_2$P/SiO$_2$ (panel a), NiFeP(3:1)/SiO$_2$ (panel b) and NiFeP(1:1)/SiO$_2$ (panel c) samples, after 40 h of lining out. The Fe$_2$P/SiO$_2$ sample deactivated in the course of reaction, as found earlier [44], thus results for this sample are not presented. Liquid feeds with two compositions were introduced in sequence during the course of the reaction test. Initially (Fig. 5, section i), 0.05% S in the form of 4,6-DMDBT, 0.3% S as DMDS, and 0.02% N as quinoline all dissolved in tridecane were introduced. The Ni$_2$P/SiO$_2$ catalyst exhibited high reactivity and stability with a 4,6-DMDBT conversion of 97–99%. The NiFeP(3:1)/SiO$_2$ sample had an HDS conversion of around 90% and showed a slight decline in activity. The NiFeP(1:1)/SiO$_2$ sample showed a much lower HDS conversion of only about 40% and also exhibited slight deactivation. With more Fe content, the activity of the catalysts became lower. This is consistent with an earlier study of dibenzothiophene HDS which showed that Fe$_2$P had a much lower intrinsic activity than Ni$_2$P [44]. After 75 h a feed with an additional 0.3% S as DMDS was introduced (Fig. 5, section ii). The activity of the Ni$_2$P/SiO$_2$ did not show much difference, however, the 4,6-DMDBT conversions on NiFeP/SiO$_2$ (3:1) and NiFeP/SiO$_2$ (1:1) decreased to 90% and 85% respectively. The small effect of sulfur on the performance of Ni$_2$P/SiO$_2$ had been reported earlier [34,67,68].

The activities of the NiFeP/SiO$_2$ samples increased to the level of the Ni$_2$P/SiO$_2$ sample, and this suggests that reconstruction occurred, leading to perhaps a Ni terminated surface, because the active surface of Ni phosphide catalysts is actually a phosphosulfide [58,67,69] and there is hydrogen present in the feed, so a driving force for the reconstruction may be the formation of Ni—S bonds at the expense of Fe—S bonds, which would be less stable in the presence of H$_2$ at high temperature. When sulfur concentration is increased (Fig. 5, section ii), this favors the formation of Fe—S, and

the activity decreased, because of the intrinsically lower activity of Fe$_2$P.

The conversions and product distributions at 613 K (340 °C) and 3.1 MPa are summarized in Table 5. The table lists the reactants, the reaction types, and the corresponding conversions and selectivities with three catalysts. The Ni$_2$P/SiO$_2$ displayed the highest activity with a 4,6-DMDBT conversion level of 99%. The HDS activity of the NiFeP(3:1)/SiO$_2$ and NiFeP(1:1)/SiO$_2$ catalysts were also very high giving a 4,6-DMDBT conversion over 95%. According to the published literature [70,71], there are three major products formed from 4,6-DMDBT conversion on the catalysts: (1) 3,3′-dimethylbiphenyl (DMBP), (2) 3-(3′-methylcyclohexyl)toluene (MCHT), and (3) 3,3′-dimethylbicyclohexyl (DMBCH). The DMBP has been considered as the product from direct desulfurization (DDS) pathway, whereas the MCHT and DMBCH from hydrogenation (HYD) pathway [72,73]. A previous study using similar condition also pointed out that DMBP cannot be produced by a secondary dehydrogenation pathway as the parallel dehydrogenation of tetralin to naphthalene did not occur [42].

Table 5 shows that the Ni$_2$P/SiO$_2$ gave a low DMBP selectivity of 12% and high MCHT and DMBCH selectivity totally accounting for 88%, indicating that Ni$_2$P/SiO$_2$ favors the HYD pathway. On the other hand, NiFeP(3:1)/SiO$_2$ and NiFeP(1:1)/SiO$_2$ catalysts showed higher DMBP selectivity than that of the hydrogenation products MCHT and DMBCH. The NiFeP(1:1)/SiO$_2$ sample even gave higher DMBP selectivity of 85% than the 69% selectivity with NiFeP(3:1)/SiO$_2$. As Fe$_2$P catalyst was found inactive for HDS of both DBT in earlier study and DMDBT in this study, the unprecedentedly high selectivity toward DDS and relatively high activity suggest that the substitution of Fe for Ni changes the electronic structure and properties of the cluster. As the DDS pathway is intrinsically more difficult than the HYD pathway for HDS of 4,6-DMDBT, this rationalizes the decrease in HDS activity in the samples with higher Fe content.

The HDN of quinoline does not occur directly because of the strength of the C—N bonds and is a complex sequential reaction involving hydrogenation of the N-ring, hydrogenolysis of the aliphatic C—N bond (CNH), hydrogenation of the C6-ring (HYD), and elimination of ammonia [74]. This may be followed by hydrogenation of the C6-ring to form propylcyclohexane (PCH) or dehydrogenation to form propylbenzene (PB). In the case of the phosphides studied here it is found that Ni$_2$P/SiO$_2$ favors formation of PCH, as also reported earlier [67,75], but increasing iron substitution in the NiFeP(3:1)/SiO$_2$ and NiFeP(1:1)/SiO$_2$ catalysts gives higher selectivity to PB, indicating that the hydrogenation ability of the Ni is suppressed by the addition of Fe. Consistently, bimetallic phosphides CoNi and FeNi phosphides were also reported higher selectivity for HDN of carbazole with more unsaturated cyclohexylbenze products than with commercial Ni–Mo catalysts [76]. On sulfides detailed kinetic studies show that the rates of HYD and CNH are of a similar order of magnitude and no single rate-limiting step is operative [77,78]. On phosphides similar studies have not been carried out, but it is likely that again no single rate-limiting step is involved, and that CNH will be one of the key steps. The CNH reaction is a complex reaction and requires multiple sites [79–81] among them an acid site to bind the nitrogen compound and a proximal basic site to carry out a β-H attack. Thus, the reaction is structure sensitive [67], and is expected to be influenced by the substitution of Fe for Ni at the surface.

3.6. EXAFS of the fresh samples

The Fourier-transformed EXAFS spectra at the Ni K-edge for the fresh Ni$_2$P/SiO$_2$, NiFeP(3:1)/SiO$_2$, NiFeP(1:1)/SiO$_2$, and NiFeP(1:3)/SiO$_2$ samples together with some reference standards, bulk Ni$_2$P and NiO are shown in Fig. 6. The bulk Ni$_2$P reference

Table 5
Conversions and selectivities of the silica-supported nickel phosphides and nickel iron phosphides at 613 K and 3.1 MPa with feed b after 110 h on stream.

Reactants	Type	Conversion (%)			Products	Selectivity (%)		
		Ni$_2$P/SiO$_2$	NiFeP(3:1)/SiO$_2$	NiFeP(1:1)/SiO$_2$		Ni$_2$P/SiO$_2$	NiFeP(3:1)/SiO$_2$	NiFeP(1:1)/SiO$_2$
4,6-DMDBT	HDS	99	99	96	3,3′-Dimethylbiphenyl	12	69	85
					3-(3′-Methylcyclohexyl)toluene	53	21	11
					3,3′-Dimethylbicyclohexyl	35	10	4
Quinoline	HDN	100	100	100	Propylcyclohexane	74	45	37
					Propylbenzene	26	55	63
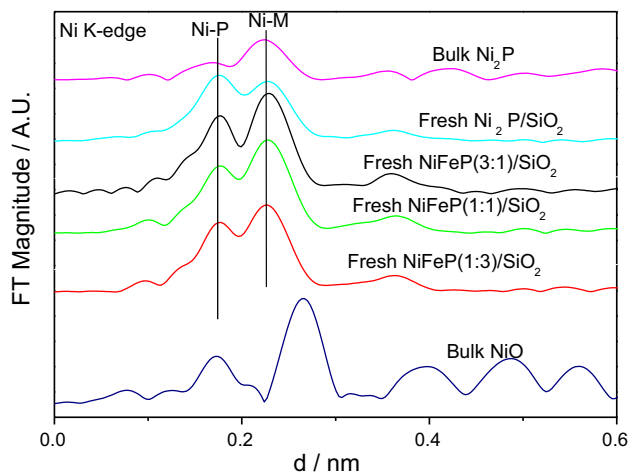
Fig. 6. Comparison of Fourier transforms of the Ni K-edge EXAFS spectra for bulk Ni$_2$P, fresh Ni$_2$P/SiO$_2$, fresh NiFeP(3:1)/SiO$_2$, fresh NiFeP(1:1)/SiO$_2$, fresh NiFeP(1:3)/SiO$_2$, bulk NiO. Ni(2) terminated Fresh Ni$_2$P/SiO$_2$

Fig. 7. Comparison of Fourier transforms of the Fe K-edge EXAFS spectra for fresh NiFeP(3:1)/SiO$_2$, fresh NiFeP(1:1)/SiO$_2$, fresh NiFeP(1:3)/SiO$_2$, fresh Fe$_2$P:SiO$_2$, bulk FeO, bulk FeS.

sample shows two peaks at distances of 0.17 nm and 0.23 nm roughly corresponding to Ni—P and Ni—Ni bond distances. The supported Ni$_2$P samples show two distinctive peaks at similar positions as the bulk Ni$_2$P but the Ni—P peak intensity in the supported Ni$_2$P is much stronger than the Ni—Ni peak. This is due to the presence of small Ni$_2$P crystallites with excess Ni(2) atoms on the surface which have a pyramidal five fold coordination of phosphorus [39,55]. The termination of the crystallites with the Ni(2) atoms as opposed to the tetrahedral Ni(1) atoms results in high phosphorus levels in the sample. The samples with Fe content also show peaks at similar bond distances. A Ni atom probed by EXAFS can have either Ni or Fe neighbors, therefore the neighboring atoms are all denoted as M. Although there is some variation from sample to sample, as the Fe content increases the Ni—M peak intensity also grows while the Ni—P intensity decreases. This is possibly due to the decreasing number of Ni(2) sites at the surface of the crystallites because of the Fe substitution for the Ni(2) site positions. Since these Ni(2) sites were found to be more active [39], the decreasing number of Ni(2) sites on the surface would account for the initial low activity of the samples containing Fe (Fig. 5, section i).

The Fourier-transform EXAFS spectra at Fe K-edge of the fresh NiFeP(3:1)/SiO$_2$, NiFeP(1:1)/SiO$_2$, NiFeP(1:3)/SiO$_2$, and Fe$_2$P/SiO$_2$ samples together with reference standards, FeS and FeO are shown in Fig. 7. The supported Fe$_2$P sample shows two peaks at distances of 0.18 nm and 0.23 nm roughly corresponding to Fe—P and Fe—Fe distances, which are similar to those of Ni$_2$P as Ni$_2$P and Fe$_2$P have the same crystal structure. The supported NiFeP samples show two peaks at similar positions as supported Fe$_2$P. However, in the higher Ni content catalysts the Fe—P peak moved from 0.18 nm to 0.17 nm and the peak intensity becomes stronger. This indicates that the Fe in the NiFe samples takes a structure with lattice parameters closer to Ni$_2$P which makes the Fe-P distance shorter. Overall, the peak intensities of the Fe-P bond were higher than those of the
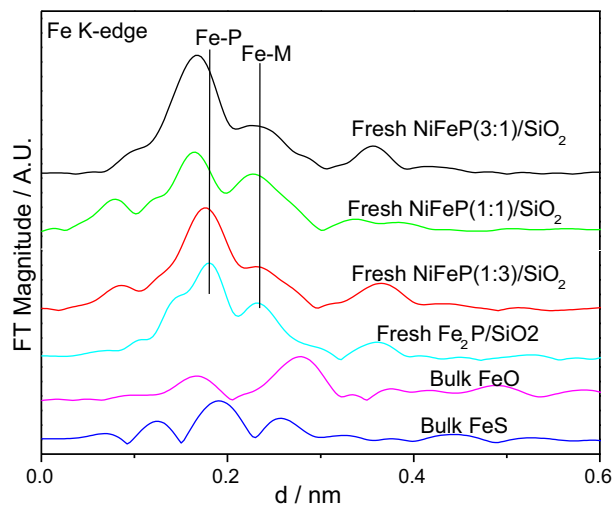
Fe-M bond, as found for the Fe$_2$P/SiO$_2$ sample, indicating that the Fe was fully phosphided.

To extract quantitative information from the EXAFS, the EXAFS data of the Ni and Fe K-edge for the samples Ni$_2$P/SiO$_2$, NiFeP(3:1)/SiO$_2$, NiFeP(1:1)/SiO$_2$, NiFeP(1:3)/SiO$_2$, and Fe$_2$P/SiO$_2$ were Fourier transformed over the data range from 20 to 120 nm^{-1} (2–12 Å^{-1}) and modeled within the region from 0.1 to 0.3 nm. A Ni K-edge EXAFS model for the Ni$_2$P/SiO$_2$ was built using FEFF7, based on the crystal structure of Ni$_2$P, and gave a reasonable fit with low R value as shown in Table S5a (Supplementary information). R stands for the residual, defined in Eq. (1).

$$R = \frac{\sum_{i=1}^{N} |y_{exp}(i_0) - y_{theo}(i)|}{\sum_{i=1}^{N} y_{exp}(i)} \tag{1}$$

The model used 7 paths including both Ni(1) and Ni(2) as absorbers, so it accounts for the known structural details from the crystallography of the compound. The model determines two energy shift parameters for M(1) and M(2) paths respectively, two Debye-Waller parameters, two expansion/contraction terms [82] for the distances to these neighboring atoms, and three scaling factors for coordination numbers, which totally contains 9 parameters. Because the number of independent fitting parameters is limited by 14 as given by the formula below [83], this model with 9 parameters is well constrained and permissible.

$$N_{ind} = \frac{2kR}{\pi} + 2 \tag{2}$$

The best fit parameters for Fe$_2$P/SiO$_2$ are shown in Table S5b by using a similar model for Ni$_2$P based on the crystal parameters for Fe$_2$P. The ratio of the scaling factor for coordination numbers of M(1) and M(2) in Ni K-edge and Fe K-edge are both 0.9 in Ni$_2$P/SiO$_2$ and Fe$_2$P/SiO$_2$ (Table 6).
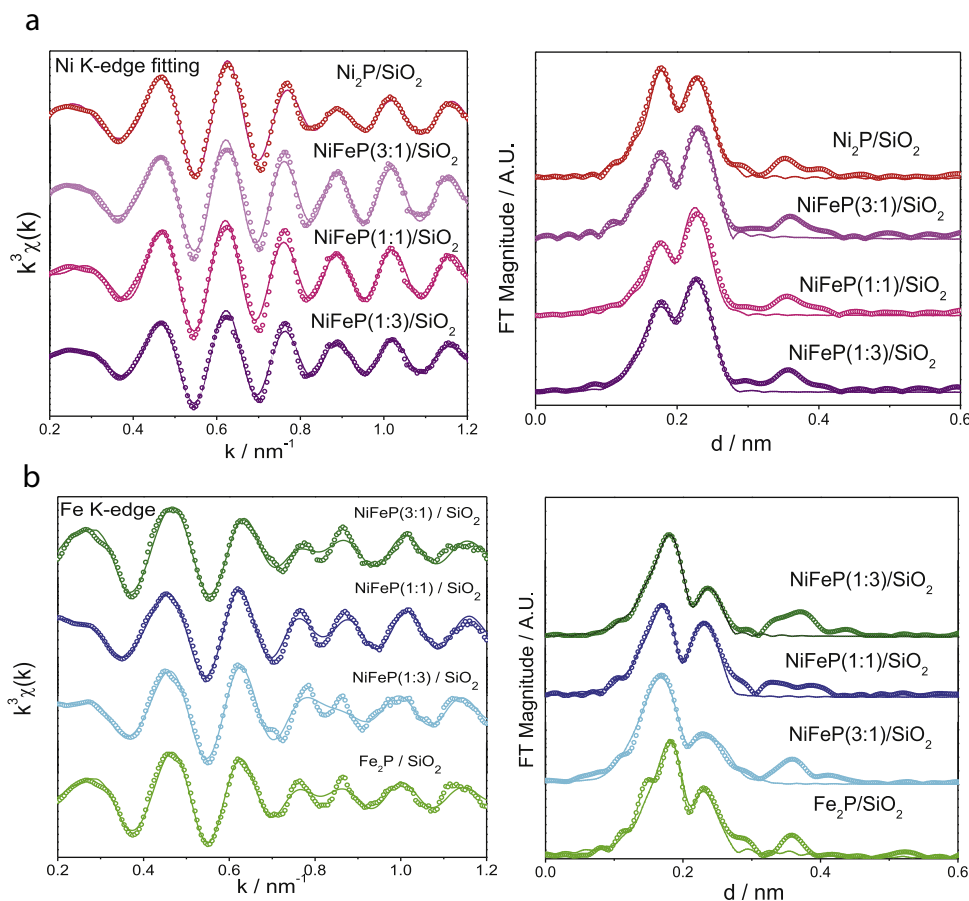
Fig. 8. (a) (Left) Ni K-edge EXAFS spectra (symbols) and model (line) from NiFeP/SiO$_2$ samples. (Right) Magnitude of the Fourier transform of the Ni K-edge spectra (symbols) and model (line) (b). (Left) Fe K-edge EXAFS spectra (symbols) and model (line) from NiFeP/SiO$_2$ samples. (Right) Magnitude of the Fourier transform of the Fe K-edge spectra (symbols) and model (line).

Table 6
Comparison of different models based on Ni(1) and Ni(2) substitution for both Ni and Fe K-edge EXAFS.

Catalyst	Ni K-edge M(1)/M(2)	Fe K-edge M(1)/M(2)
Ni$_2$P/SiO$_2$	0.9	N/A
NiFeP(3:1)/SiO$_2$	0.8	0.7
NiFeP(1:1)/SiO$_2$	1.5	0.6
NiFeP(1:3)/SiO$_2$	1.3	0.8
Fe$_2$P/SiO$_2$	N/A	0.9

The EXAFS spectra of the Ni K-edge for NiFeP(3:1)/SiO$_2$, NiFeP(1:1)/SiO$_2$, and NiFeP(1:3)/SiO$_2$ were fit with a model of Ni$_2$P as the NiFeP alloy has a very similar crystal structure to Ni$_2$P (Tables S6a–S8a), and the resulting FT spectra for the best fit models are plotted in Fig. 8a. The Fe K-edge fitting results are shown in Tables S6b–S8b and the resulting FT spectra for the best fit models are plotted in Fig. 8b. Except for the sample NiFeP(3:1)/SiO$_2$, the ratio of M(1)/M(2) for the Ni K-edge in the bimetallic phosphides samples are bigger than 0.9 for the pure Ni$_2$P/SiO$_2$, suggesting Ni occupies more tetrahedral (T) M(1) sites in the low Fe content NiFeP/SiO$_2$ than in Ni$_2$P/SiO$_2$. Correspondingly, the ratio of M(1)/M(2) for the Fe K-edge in these bimetallic phosphides samples are generally smaller than in pure Fe$_2$P/SiO$_2$, suggesting Fe occupies more square pyramidal (SP) M(2) sites, which is consistent with the results of the Ni K-edge modeling. The exception is the sample NiFeP(3:1)/SiO$_2$, where the ratio of M(1)/M(2) for both the Ni K-edge and Fe K-edge are smaller than 0.9, which imply that both Ni and Fe prefer M(2) positions.

In summary, the substitution of Fe for Ni most likely occurs on the square pyramidal Ni(2) sites in the catalysts NiFeP(1:1)/SiO$_2$, NiFeP(1:3)/SiO$_2$. Since the Ni(2) sites are more active than the Ni(1) sites, this explains the decrease in HDS activity of NiFeP(1:1)/SiO$_2$ compared to that of Ni$_2$P/SiO$_2$ (Fig. 5, section i). The substitution of Fe in the Ni(1) and Ni(2) sites show similar probabilities in the catalyst NiFeP(3:1)/SiO$_2$. According to the principle of efficient space filling [84,85], the larger metal atoms should preferentially occupy the M(2) position with the highest coordination number. The metallic bond radii of Ni and Fe are 0.125, 0.126 nm respectively, which are fairly close and make the situation complex to determine the Fe position in the alloys. It has been reported that the equilibrium distribution of iron atoms over the tetrahedral site M(1) and pyramidal site M(2) depends on the chemical composition of Fe$_x$Ni$_{1-x}$P$(0 < x < 1)$ [61]: for the Fe-rich materials $(x \geq 0.45)$, Fe atoms favors more M(2) sites than M(1); for the Ni-rich materials $(x \leq 0.15)$, for example, FeNiP(0.15:0.85), the Fe will occupy exclusive M(1) sites. This is consistent with the NiFeP/SiO$_2$ samples in this study. Moreover, samples with smaller contents of Fe, less than 15%, are worthwhile for further investigation.

3.7. Density functional theory calculations

The construction of various NiFeP unit cells starts with Ni$_2$P and Fe$_2$P structures which belong to the hexagonal $P\bar{6}2m$ space symmetry group [86,87] with atoms located in four symmetry non-equivalent sites (Fig. 1). Metal atoms $P\bar{6}2m$ occupy three symmetry equivalent tetrahedral sites (T) and three symmetry equivalent square pyramidal (SP) sites. The site T denotes crystallographic
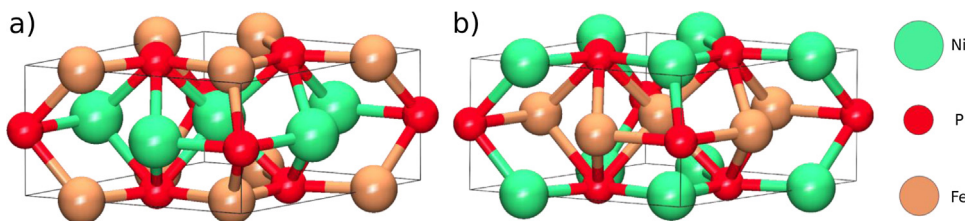
Fig. 9. Hexagonal NiFeP structures with (a) Ni in T and Fe in SP sites and (b) Fe in SP and Ni in T sites; in both structures P_1 and P_2 sites are occupied by P atoms.

positions $x_1 0\,0$, $0x_1 0$, $\bar{x}_1\bar{x}_1 0$ with x_1 referred hereafter as T crystallographic coordinate and SP denotes crystallographic positions $x_2\,0\frac{1}{2}$, $0x_2\frac{1}{2}$, $\bar{x}_2\bar{x}_2\frac{1}{2}$ with x_2 referred hereafter as SP crystallographic coordinate. Phosphorus atoms are situated in one P_1 site $0\,0\frac{1}{2}$ and two P_2 sites $\frac{1}{3}\frac{2}{3}0$ and $\frac{2}{3}\frac{1}{3}0$.

Substituting three symmetry equivalent Fe atoms in the Fe_2P unit cell by Ni atoms it is possible to generate NiFeP structures which still belong to the D_{3h} symmetry point group. Two different atom arrangements are possible because there are two symmetry non-equivalent Fe sites (Fig. 9). Similarly, substitution of three symmetry equivalent Ni atoms by Fe atoms is possible for the Ni_2P structure.

Structures with mixed Fe–Ni tetrahedral sites occupancies are formed by exchanging positions of Fe and Ni atoms within NiFeP structure. Two different atom arrangements are possible for both 67% Fe–33% Ni and 33% Fe–67% Ni tetrahedral sites occupancies (Fig. 10). For 50% Fe–50% Ni tetrahedral sites occupancies all possible structures (about 400) were constructed using $1 \times 1 \times 2$ FeNiP supercell (Fig. 11).

Three sets of cell parameters were used for calculations on the NiFeP system: (i) experimental and DFT optimized values for Fe_2P, (ii) experimental and DFT optimized values for Ni_2P, and (iii) DFT optimized values for NiFeP. For each choice of the unit cell parameters the atomic positions were optimized.

Table 7 compares experimental and calculated structure parameters for hexagonal Fe_2P, Ni_2P and NiFeP. The calculated structures show less than 1% deviation from the experimental data.

Calculation results for various choices of NiFeP structures with fractional occupations of T and SP sites are shown in Table 8. The most stable structures contain 50% Fe atoms in tetrahedral positions and are energetically preferred over other investigated configurations by at least 1.5 kJ/mol per atom. This energy

difference is not very large. It is worth pointing out that metal atoms in the most stable structures do not mix within a single square pyramidal layer. Instead, metal atoms are aligned in alternate Ni–P and Fe–P layers (Fig. 11).

A model of the structure of a fresh NiFeP(1:1) catalyst is presented in Fig. 12 [88]. It consists of sequential layers of T and SP structure, which are alternately occupied by Ni and Fe atoms (Fig. 11). The bulk structure contains equal numbers of T and SP sites but the nanoparticles can have unequal numbers depending on the termination. In this case the surface is terminated by tetrahedral M(1) sites, and these are preferentially occupied by Ni sites, as shown by EXAFS. This gives rise to enhanced selectivity to the direct desulfurization product, dimethylbiphenyl. We acknowledge that we cannot explain the termination structure at the present time, as this would entail calculation of particles with hundreds of metal atoms, which is beyond our present capabilities. If the termination can be controlled, for example by alloying, there could be possibility of control of reaction rate and selectivity as the HDS reaction for hindered molecules like DMDBT is structure-sensitive [34].

3.8. EXAFS analysis of the spent samples

Fig. 13 shows the EXAFS data for the NiFeP(1:1)/SiO_2 sample before and after reaction together with FeS as reference. This sample was chosen for analysis because it showed the greatest change in activity in the course of activation (Fig. 5, panel b). For the Ni-edge (Fig. 13a) the fresh sample shows a strong Ni—M peak intensity relative to the Ni—P peak, while the spent sample shows a reduced Ni—M peak intensity with maintenance of the Ni—P intensity. For the Fe K-edge (Fig. 13b) the fresh sample shows a stronger Fe—P peak intensity relative to the Fe—M peak, while the spent sample shows a decreased Fe—M intensity with maintenance of the
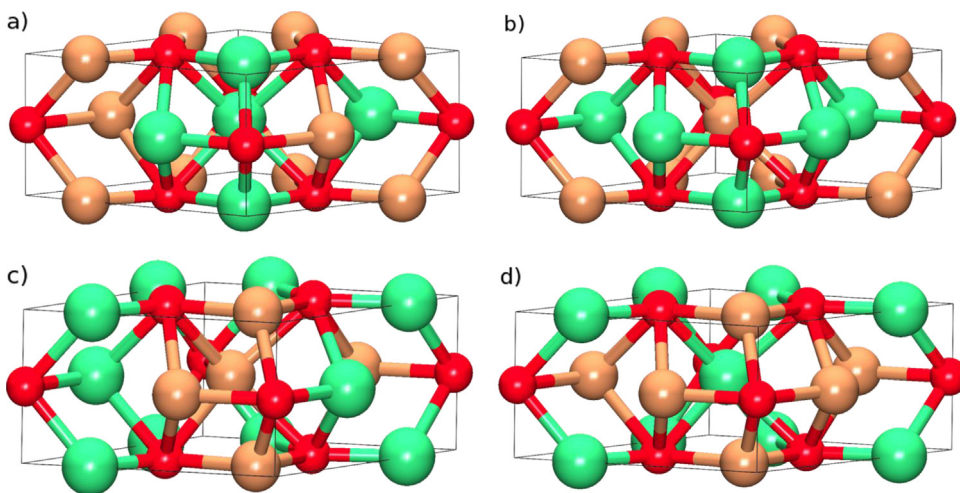

Fig. 10. NiFeP structures with 66% of Fe atoms in tetrahedral sites: (a) C_{1h} symmetry, (b) C_{2v} symmetry. NiFeP structures with 33% of Fe atoms in tetrahedral sites: (c) C_{1h} symmetry, (d) C_{2v} symmetry. For color coding, see Fig. 1. (For interpretation of the references to color in this figure legend, the reader is referred to the web version of this article.)
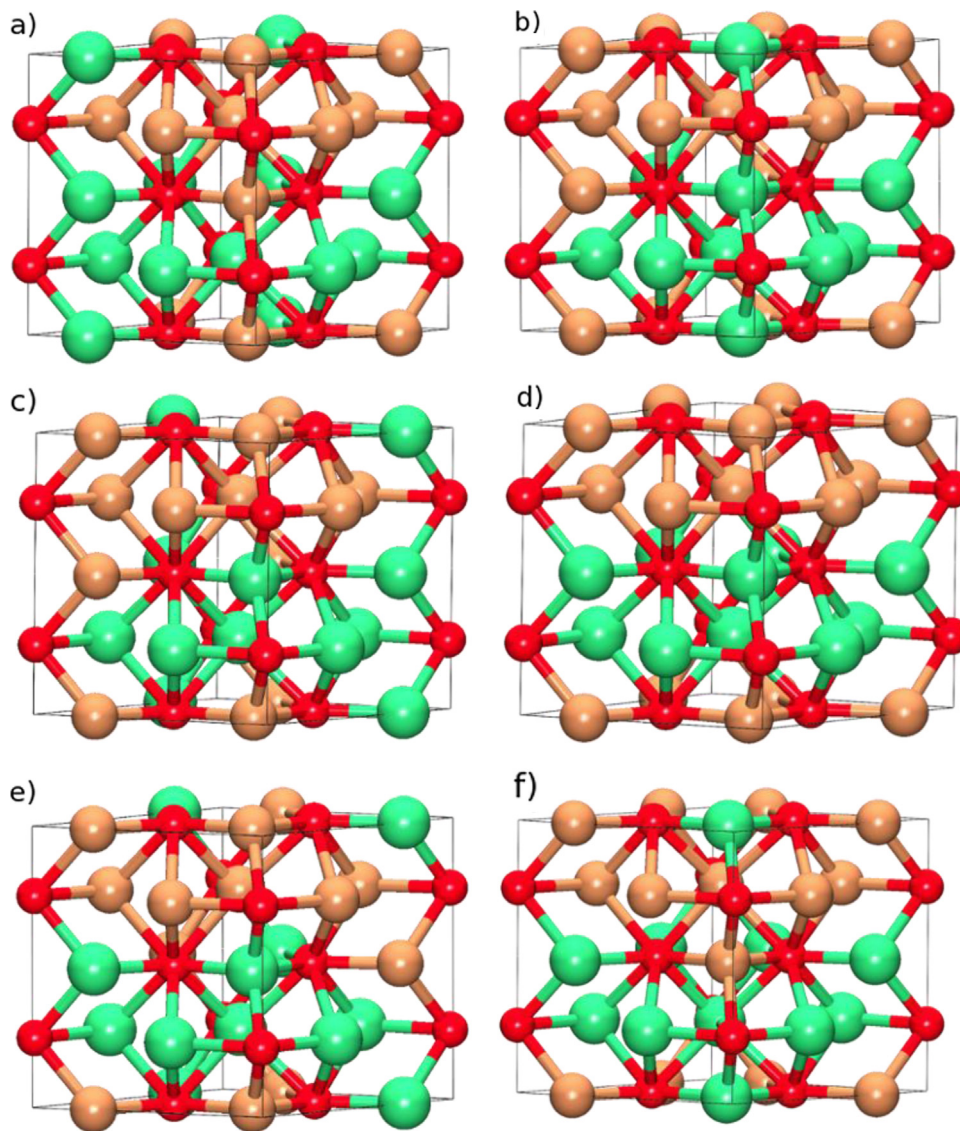
Fig. 11. The most stable NiFeP structures with 50% Fe – 50% Ni tetrahedral sites occupancies. For color coding, see Fig. 1. (For interpretation of the references to color in this figure legend, the reader is referred to the web version of this article.)

Table 7
Comparison of experimental and calculated Fe_2P, Ni_2P and NiFeP hexagonal structures. Set denotes the type of unit cell (see text for details). ΔE denotes relative energies of the two arrangements of Ni and Fe atoms within a given unit cell.

Set	Cell parameters (Å)		Crystallographic coordinate		ΔE (kJ/mol/atom)
	a	c	T	SP	
Fe₂P			Fe 0.256[a]	Fe 0.594[a]	
	5.865[a]	3.456[a]	Fe 0.2601	Ni 0.6034	0.0
			Ni 0.2589	Fe 0.6021	1.37
			Fe 0.2570	Fe 0.5909	
	5.809[b]	3.428[b]	Fe 0.2597	Ni 0.6023	0.0
			Ni 0.2580	Fe 0.6006	1.17
Ni₂P			Ni 0.2575[c]	Ni 0.5957[c]	
	5.859[c]	3.382[c]	Fe 0.2606	Ni 0.6031	0.0
			Ni 0.2594	Fe 0.6021	1.51
			Ni 0.2598	Ni 0.6013	
	5.886[b]	3.372[b]	Fe 0.2610	Ni 0.6035	0.0
			Ni 0.2600	Fe 0.6029	1.62
NiFeP[b]	5.841	3.364	Fe 0.2606	Ni 0.6029	0.0
	5.790	3.408	Ni 0.2578	Fe 0.6001	1.30

[a] Ref. [86].
[b] Calculated unit cell parameters.
[c] Ref. [87].

Table 8
Comparison of chosen calculated NiFeP structures with fractional occupations of T and SP sites.

% Fe in T	Cell parameters (Å)		ΔE (kJ/mol/atom)
	a	c	
66% (Fig. 10a)			−0.85
66% (Fig. 10b)			−0.08
33% (Fig. 10c)	5.841[a]	3.364[a]	0.57
33% (Fig. 10d)			−0.27
50% (Fig. 11a)			−1.60
50% (Fig. 11b)			−1.60
50% (Fig. 11c)	5.841[b]	6.729[b]	−1.60
50% (Fig. 11d)			−1.57
50% (Fig. 11e)			−1.49
50% (Fig. 11f)			−1.49

ΔE denotes relative energies with respect to the energy of the most stable hexagonal FeNiP structure (cf. Fig. 11). Only the most stable structures of a given type are presented.

[a] Cell parameters of the energetically most stable hexagonal FeNiP structure.
[b] $1 \times 1 \times 2$ supercell.

Fe—P intensity. The lowering of the Ni—M and Fe—M intensity is consistent with disruption of metal–metal bonds because of formation of a surface sulfide. A schematic of the transformation to the active phase is depicted in Fig. 7. In order to analyze the data further [89] a difference spectra of the Fe and Ni K-edge spectra are taken between the fresh and spent NiFeP(1:1)/SiO₂ sample as shown in Fig. 13c and d. A set of oscillations is obtained. It is assumed here that the structure of the catalyst in the working state does not change very much on quenching and that the catalyst sample referred to as spent retains its most important features. Indeed, the in situ EXAFS studies of an active Ni₂P catalyst show that
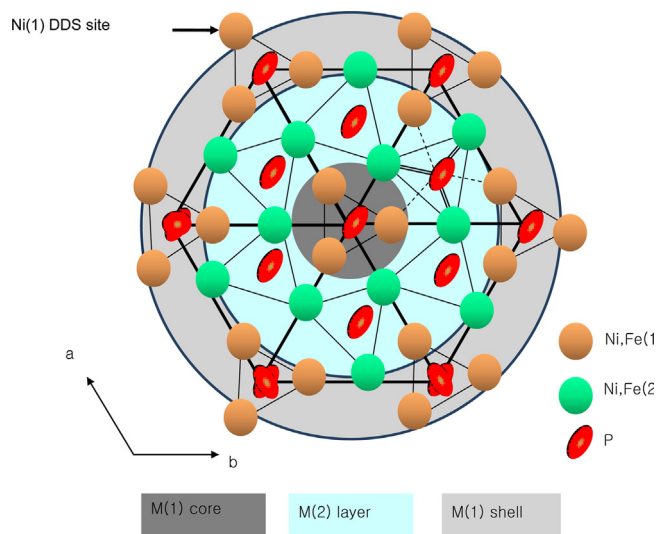

Fig. 12. Cross sectional schematic model of phosphide crystallites in Ni₂P/SiO₂ and NiFeP(1:1)/SiO₂.

the Ni₂P structure is retained in the bulk and that Ni—S bonds are observed on the surface [90]. The fact that the oscillations in Fig. 13 are centered around zero indicate that the subtraction has been successful. The difference spectra are fitted with F_{eff} using Fe—S and Ni—S bonds at distances of 0.226 and 0.238 nm, which are typical of these bonds. The bond length of Fe_xS_y varies between 0.221 and 0.246 nm (0.226 nm for FeS [91], 0.221 [92] and 0.225 nm in FeS₂ [93], 0.214 and 0.246 nm in Fe₃S₄ [94]). In typical Ni_xS_y compounds, Ni—S bonds are found in the range of 0.225–0.240 nm (0.238 nm
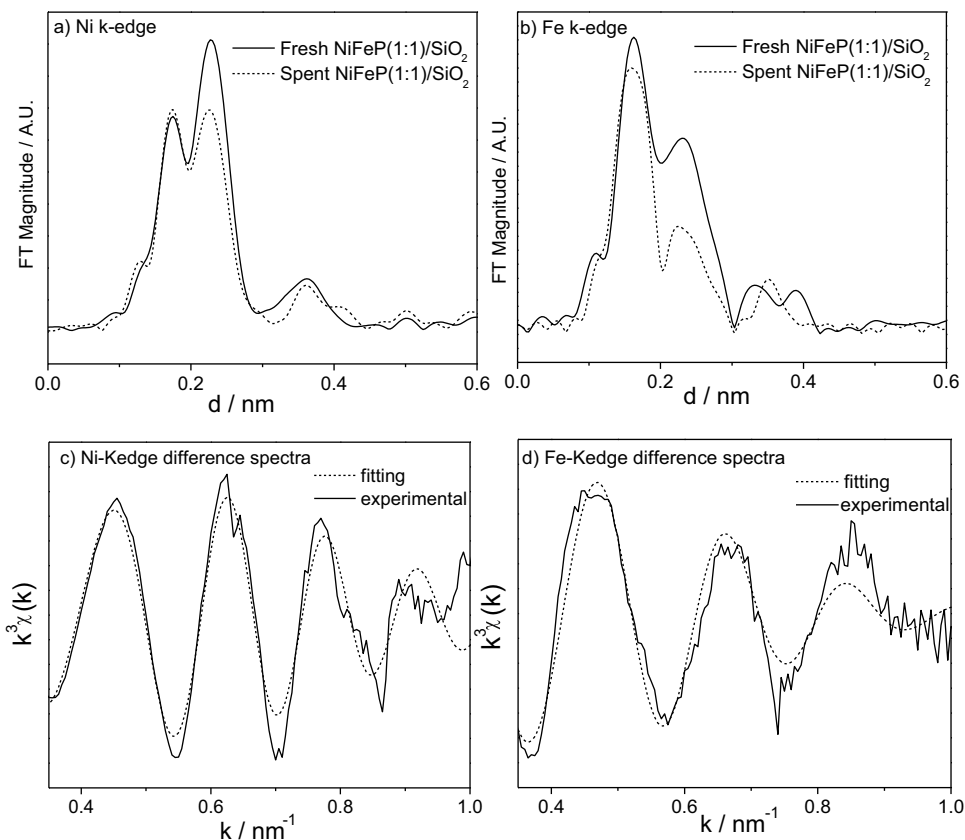

Fig. 13. (a) Ni K-edge EXAFS spectra for fresh and spent NiFeP(1:1)/SiO₂. (b) Fe K-edge EXAFS spectra for fresh and spent NiFeP(1:1)/SiO₂. (c) Ni K-edge difference spectra. (d) Fe K-edge difference spectra.

for NiS [95], 0.236 nm for NiS_2 [96], and 0.225 and 0.229 nm for Ni_3S_2 [97]). The good fit clearly shows that Fe—S and Ni—S bonds are present in the spent sample, confirming the formation of a phosphosulfide. There are also more oscillation peaks at the Ni K-edge than at the Fe K-edge, which indicates that more Ni—S is formed than Fe—S. Many studies [98–100] have shown that the active phase is a phosphosulfide. It has been found that small amounts of Co in Ni_xCo_yP catalysts are promoters [33], and it should be interesting to probe the reactivity of small amounts (<15 mol%) of Fe in NiFeP catalysts.

In summary, the nature of the active sites in Ni_2P HDS catalysts was studied by forming NiFeP alloys and by correlating the reactivity behavior with the surface properties and the compositions of the different phases. The Ni_2P structure (hexagonal, $P\bar{6}2m$) has two types of Ni, a tetrahedrally (T) coordinated Ni(1) and a square pyramidal (SP) coordinated Ni(2), and previous work [39] had indicated that the Ni(2) site was the active center for HDS by the hydrogenation route. Fe_2P has the same crystal structure as Ni_2P, but is an inactive phase probably because it forms strong Fe—S bonds, so Fe was deemed as a good diluent in the Ni_2P phase to probe the sites. Indeed FTIR spectra of adsorbed CO showed a gradual progression to lower wavenumber as Fe was added to the Ni_2P phase. In its reactivity behavior at 340 °C, the NiFeP(3:1)/SiO_2 and NiFeP(1:1)/SiO_2 samples both showed high activity close to that of Ni_2P/SiO_2, but with much higher selectivity for the direct desulfurization product dimethybiphenyl. This suggested the presence of Ni(1) sites at the surface, and a model was proposed based on DFT and EXAFS results of nanoparticles with alternating tetrahedral and square pyramidal sites, terminated by pyramidal sites.

4. Conclusions

The purpose of this work was to understand the nature of the active sites in Ni_2P hydrodesulfurization (HDS) catalysts by the alloying with Fe, an inactive element. The catalysts studied were Ni_2P/SiO_2, NiFeP(3:1)/SiO_2, NiFeP(1:1)/SiO_2, NiFeP(1:3)/SiO_2, and Fe_2P/SiO_2. The main findings were as follows:

1) Characterization of the catalysts by CO chemisorption and X-ray diffraction line broadening analysis indicates crystallites of size less than 10 nm, and increasing occupation of the surface with Fe as the overall Fe content increases.
2) Study of the catalysts by Fourier transform infrared (FTIR) spectroscopy using CO as a probe showed a gradual diminution in the CO stretching frequency, indicating that the Fe component has electron donating properties.
3) At 613 K (340 °C) Ni_2P has excellent activity for the simultaneous HDS of 4,6-dimethyldibenzothiophene (conversion 99%) and the hydrodenitrogenation of quinoline (conversion 100%). The substitution of Fe for Ni decreases the activity only slightly, but greatly increases the selectivity for the direct desulfurization (DDS) route. The DDS route had earlier been associated with tetrahedral Ni(1) sites.
4) Analysis by extended X-ray absorption fine structure (EXAFS) analysis of the fresh samples indicates that the Fe preferentially substitutes for square pyramidal (SP) Ni sites (denoted as Ni(2) sites) instead of tetrahedral (T) Ni sites (denoted as Ni(1) sites).
5) Density functional theory calculations indicate that in the bulk there is no preferential occupation of T and SP sites by Fe over Ni.
6) The nanosize NiFe particles consist of layers of SP and T sites that terminate with T sites explaining the high selectivity to the DDS product.

7) A reconstruction of the bimetallic catalysts occurs at reaction conditions that produce an active phosphosulfide phase with both Ni—S and Fe—S bonds.

Appendix A. Supplementary data

Supplementary data associated with this article can be found, in the online version, at http://dx.doi.org/10.1016/j.apcatb.2014.09.010.

References

[1] M. Marafi, A. Stanislaus, E. Furimsky, Handbook of Spent Hydroprocessing Catalysts, 2010, pp. 17–49 (Chapter 3).
[2] J. Ancheyta, F. Trejo, M.S. Rana, Asphaltenes Chemical Transformation During Hydroprocessing of Heavy Oils, Taylor & Francis, New York, 2010.
[3] G. Hess, Chem. Eng. News 92 (2014) 28.
[4] P. Castillo-Villalón, J. Ramirez, R. Castañeda, J. Catal. 294 (2012) 54.
[5] R. Huirache-Acuña, B. Pawelec, C.V. Loricera, E.M. Rivera-Muñoz, R. Nava, B. Torres, J.L.G. Fierro, Appl. Catal. B: Environ. 125 (2012) 473.
[6] P. Rayo, J. Ramírez, P. Torres-Mancera, G. Marroquín, S.K. Maity, J. Ancheyta, Fuel 100 (2012) 34.
[7] J.N. Díaz de León, M. Picquart, L. Massin, M. Vrinat, J.A. de los Reyes, J. Mol. Catal. A: Chem. 363–364 (2012) 311.
[8] B. Liu, Y. Chai, Y. Liu, Y. Wang, Y. Liu, C. Liu, Fuel 95 (2012) 457.
[9] C. Leyva, J. Ancheyta, A. Travert, F. Maugé, L. e Mariey, J. Ramírez, M.S. Rana, Appl. Catal. A: Gen. 425–426 (2012) 1.
[10] E. Kraleva, A. Spojakina, M.L. Saladino, E. Caponetti, G. Nasillo, K. Jiratova, J. Alloys Compd. 513 (2012) 310.
[11] S. Yao, Y. Zheng, S. Ng, L. Ding, H. Yang, Appl. Catal. A: Gen. 435–436 (2012) 61.
[12] Y. Li, D. Pan, C. Yu, Y. Fan, X. Bao, J. Catal. 286 (2012) 124.
[13] K.K. Soni, K. Chandra Mouli, A.K. Dalai, J. Adjaye, Microporous Mesoporous Mater. 152 (2012) 224.
[14] E. Torres-García, A. Galano, G. Rodriguez-Gattorno, J. Catal. 282 (2011) 201.
[15] V.G. Baldovino-Medrano, P. Eloy, E.M. Gaigneaux, S.A. Giraldo, A. Centeno, J. Catal. 267 (2009) 129.
[16] H. Song, J. Wang, Z. Wang, H. Song, F. Li, Z. Jin, J. Catal. 311 (2014) 257.
[17] V. Teixeira da Silva, L.A. Sousa, R.M. Amorimb, L. Andrini, S.J.A. Figueroa, F.G. Requejo, F.C. Vicentini, J. Catal. 279 (2011) 88.
[18] A. Infantes-Molina, J.A. Cecilia, B. Pawelec, J.L.G. Fierro, E. Rodríguez-Castellón, A. Jiménez-López, Appl. Catal. A 390 (2010) 253.
[19] S.J. Sawhill, K.A. Layman, D.R. Van Wyk, M.H. Engelhard, C. Wang, M.E. Bussell, J. Catal. 231 (2005) 300.
[20] R. Prins, M.E. Bussell, Catal. Lett. 142 (2012) 1413.
[21] J. Wang, H. Chen, Y. Fu, J. Shen, Appl. Catal. B 104 (2011) 229.
[22] Y. Zhao, M. Xue, M. Cao, J. Shen, Appl. Catal. B 160–161 (2014) 344.
[23] X. Wang, Y. Lee, W.J. Chun, S.T. Oyama, F. Requejo, J. Catal. 210 (2002) 207.
[24] P. Clark, X. Wang, S.T. Oyama, J. Catal. 207 (2002) 256.
[25] F. Sun, W. Wu, Z. Wu, J. Guo, Z. Wei, Y. Yang, Z. Jiang, F. Tian, C. Li, J. Catal. 228 (2004) 298.
[26] C. Stinner, R. Prins, Th. Weber, J. Catal. 202 (2001) 187.
[27] J.A. Rodriguez, J.-Y. Kim, J.C. Hanson, S.J. Sawhill, M.E. Bussell, J. Phys. Chem. B (2003) 6276.
[28] D. Ma, T. Xiao, S. Xie, W. Zhou, S.L. Gonzalez-Cortes, M.L.H. Green, Chem. Mater. 16 (2004) 2697.
[29] I.I. Abu, K.J. Smith, J. Catal. 241 (2006) 356.
[30] I.I. Abu, K.J. Smith, Catal. Today 125 (2007) 248.
[31] V. Zuzaniuk, R. Prins, J. Catal. 219 (2003) 85.
[32] I.I. Abu, K.J. Smith, Appl. Catal. A: Gen. 328 (2007) 58.
[33] A.W. Burns, A.F. Gaudette, M.E. Bussell, J. Catal. 260 (2008) 262.
[34] Y. Shu, Y.K. Lee, S.T. Oyama, J. Catal. 236 (2005) 112.
[35] Q. Li, X. Hu, Phys. Rev. B 74 (2006) 35414.
[36] H. Ariga, M. Kawashima, S. Takakusagi, K. Asakura, Chem. Lett. 42 (2013) 1481–1483.
[37] J.A. Rodriguez, J.-Y. Kim, J.C. Hanson, S.J. Sawhill, M.E. Bussell, J. Phys. Chem. B 107 (2003) 6276.
[38] J.-S. Moon, E.-G. Kim, Y.-K. Lee, J. Catal. 311 (2014) 144.
[39] S.T. Oyama, Y.K. Lee, J. Catal. 258 (2008) 393.
[40] J.B. Goodenough, J. Appl. Phys. 40 (1969) 1250.

[41] J.P. Sénateur, A. Rouault, P. L'Héritier, A. Krumbügel-Nylund, R. Fruchart, D. Fruchart, P. Convert, E. Roudaut, Mater. Res. Bull. 8 (1973) 229.
[42] S.T. Oyama, H. Zhao, H.-J. Freund, K. Asakura, R. Włodarczyk, M. Sierka, J. Catal. 285 (2012) 1–5.
[43] J.F. Deng, H. Li, W. Wang, Catal. Today 51 (1999) 113.
[44] X. Wang, P. Clark, S.T. Oyama, J. Catal. 208 (2002) 321.
[45] B. Ravel, M. Newville, J. Synchrotron Rad. 12 (2005) 537.
[46] J.J. Rehr, R.C. Albers, Rev. Mod. Phys. 72 (2000) 621.
[47] S. Ramanathan, S.T. Oyama, J. Phys. Chem. 99 (1995) 16365.
[48] G. Kresse, J. Hafner, Phys. Rev. B 47 (1993) 558.
[49] G. Kresse, J. Furthmüller, Comput. Mater. Sci. 6 (1996) 15.
[50] J.P. Perdew, K. Burke, M. Ernzerhof, Phys. Rev. Lett. 77 (1996) 3865.
[51] P.E. Blöchl, Phys. Rev. B 50 (1994) 17953.
[52] G. Kresse, D. Joubert, Phys. Rev. B 59 (1999) 1758.
[53] H.J. Monkhorst, J.D. Pack, Phys. Rev. B 13 (1976) 5188.
[54] H. Fujii, S. Komura, T. Takeda, T. Okamoto, Y. Ito, J. Akimitsu, J. Phys. Soc. Jpn. 46 (1979) 1616.
[55] R. Fruchart, A. Roger, J.P. Senateur, J. Appl. Phys. 40 (1969) 1250.
[56] A. Gaudette, A.W. Burns, J.R. Hayes, M.C. Smith, R.H. Bowker, T. Seda, M.E. Bussell, J. Catal. 272 (2010) 18.
[57] K.I. Hadjiivanov, G.N. Vayssilov, Adv. Catal. 47 (2002) 307.
[58] K.A. Layman, M.E. Bussel, J. Phys. Chem. B 108 (2004) 10930.
[59] A.W. Burns, K.A. Layman, D.H. Bale, M.E. Bussell, Appl. Catal. A: Gen. 343 (2008) 68.
[60] S.J. Sawhill, K.A. Layman, D.R. Van Wyk, M.H. England, C. Wang, M.E. Bussell, J. Catal. 231 (2005) 300.
[61] Y.K. Lee, S.T. Oyama, J. Catal. 239 (2006) 376.
[62] E. Boellaard, A.M. van der Kraan, J.W. Geus, Appl. Catal. A: Gen. 224 (2002) 1.
[63] M. Lepage, T. Visser, F. Soulimani, A.M. Beale, A. Iglesias-Juez, A.M.J. van der Eerden, B.M. Weckhuysen, J. Phys. Chem. C 112 (2008) 9394.
[64] P.E.R. Blanchard, A.P. Grosvenor, R.G. Cavell, A. Mar, J. Mater. Chem. 19 (33) (2009) 6015.
[65] H. Topsøe, B.S. Clausen, F.E. Massoth, J.R. Anderson, M. Boudard, Catalysis Science and Technology, vol. 11, Springer-Verlag, New York, 1996.
[66] J.A. Rodriguez, J. Phys. Chem. B 101 (1997) 7524.
[67] S.T. Oyama, X. Wang, Y.K. Lee, K. Bando, F.G. Requejo, J. Catal. 210 (2002) 207.
[68] S.T. Oyama, J. Catal. 2106 (2003) 343.
[69] A.E. Nelson, M. Sun, A.S.M. Junaid, J. Catal. 241 (2006) 188.
[70] V. Vanrysselberghe, G.F. Froment, Ind. Eng. Chem. Res. 35 (1996) 3311.
[71] V. Vanrysselberghe, R.L. Gall, G.F. Froment, Ind. Eng. Chem. Res. 37 (1235) (1998).
[72] J.H. Kim, X. Ma, C. Song, Y.-K. Lee, S.T. Oyama, Energy Fuels 19 (2005) 353.
[73] R. Prins, M. Egorava, A. Rothlishberger, Y. Zhao, N. Sivasankar, P. Kukula, Catal. Today 111 (84) (2006).
[74] G. Perot, Catal. Today 10 (1991) 447.
[75] R. Prins, M. Jian, M. Flechsenhar, Polyhedron 16 (1997) 3235.
[76] R.H. Bowker, B.A. Carrillo, B. Ilic, M.A. Reynolds, M.E. Bussell, Appl. Catal. A 482 (2014) 221.
[77] B.K. Hodnett, B. Delmon, Stud. Surf. Sci. Catal. 27 (1986) 53.
[78] I.A. van Parijs, G.F. Froment, B. Delmon, Bull. Soc. Chim. Belg. 93 (1984) 823.
[79] J.A. Marzari, S. Rajagopal, R. Miranda, J. Catal. 156 (1995) 255.
[80] M. Jian, R. Prins, J. Catal. 179 (1998) 18.
[81] F. Rota, R. Prins, J. Mol. Catal. A 162 (2000) 359.
[82] S.D. Kelly, N. Yang, G.E. Mickelson, N. Greenlay, E. Karapetrova, W. Sinkler, S.R. Bare, J. Catal. 263 (2009) 16.
[83] E.A. Stern, Phys. Rev. B 48 (1993) 9825.
[84] Y. Maeda, Y. Takashima, J. Inorg. Nucl. Chem. 35 (1973) 1963.
[85] R.C. Buchanan, T. Park, Materials Crystal Chemistry, Mrcel Dekker Inc., 1997.
[86] S. Rundqvist, F. Jellinek, Acta Chem. Scand. 13 (1959) 425.
[87] S. Rundqvist, Acta Chem. Scand. 16 (1962) 992.
[88] J. Ren, C.F. Huo, X.D. Wen, Z. Cao, J. Wang, Y.W. Li, H. Jiao, J. Phys. Chem. B 110 (2006) 22563–22569.
[89] T. Kawai, K.K. Bando, Y.-K. Lee, S.T. Oyama, W.-J. Chun, K. Asakura, J. Catal. 241 (2006) 20.
[90] T. Kawai, W.J. Chun, K. Asakura, Y. Koike, M. Nomura, K.K. Bando, S.T. Oyama, H. Sumiya, Rev. Sci. Instrum. 79 (2008) 014101-1.
[91] A.R. Lennie, S.A.T. Redfern, P.F. Schofield, D.J. Vaughan, Mineral. Mag. 59 (1995) 677.
[92] M.J. Buerger, Am. Mineral. 16 (1931) 361.
[93] M. Rieder, J.C. Crelling, O. Sustai, M. Drabek, Z. Weiss, M. Klementova, Int. J. Coal Geol. 71 (2007) 115.
[94] B.J. Skinner, R.C. Erd, F.S. Grimaldi, Am. Mineral. 49 (1964) 543.
[95] J. Trahan, R.G. Goodrich, S.F. Watkins, Phys. Rev. B 2 (1970) 2859.
[96] T. Fujii, K. Tanaka, F. Marumo, Y. Noda, Miner. J. 13 (1987) 448.
[97] J.B. Parise, Acta Crystallogr. B 36 (1179) (1980).
[98] S.T. Oyama, X. Wang, Y.K. Lee, W.J. Chun, J. Catal. 221 (2004) 263.
[99] T. Kawai, K.K. Bando, Y.K. Lee, S.T. Oyama, W.J. Chun, K. Asakura, J. Catal. 242 (2006) 20.
[100] Y.K. Lee, Y. Shu, S.T. Oyama, Appl. Catal. A: Gen. 322 (2007) 191.